Three-Coordinate Nickel and Metal-Metal Interactions in a Heterometallic Iron-Sulfur Cluster

Daniel W. N. Wilson,[†a] Majed S. Fataftah,[†a] Zachary Mathe,[†b] Brandon Q. Mercado,[a] Serena DeBeer,[*b] and Patrick L. Holland[*a]

[a]Department of Chemistry, Yale University, 225 Prospect St., New Haven, Connecticut 06520, USA

[b]Max Planck Institute for Chemical Energy Conversion, Stiftstrasse 34-36, 45470 Mülheim an der Ruhr, Germany

[†]These three authors contributed equally.

*email: serena.debeer@cec.mpg.de; patrick.holland@yale.edu

Abstract

Biological multielectron reactions often utilize metalloenzymes with heterometallic sites, such as anaerobic carbon monoxide dehydrogenase (CODH) which has a nickel-iron-sulfide cubane with an unprecedented three-coordinate nickel site. Here, we isolate synthetic iron-sulfur clusters with three-coordinate nickel, which also have tungsten in one vertex. EPR, Mössbauer, and SQUID data are combined with DFT computations to show how the electronic structure arises from magnetic coupling between the Ni, Fe, and W sites. X-ray absorption spectroscopy favors a description as nickel(I) in two oxidation levels. Spectroscopically validated density-functional theory (DFT) calculations indicate that two electrons are stored in a nonpolar Ni–W bond. Because of the Ni–W bond, the nickel(I) site does not have substantial unpaired spin density. This gives insight into previous measurements on CODH, and generally suggests that metalloenzymes could store redox equivalents and stabilize low-valent metal centers through metal-metal bonding.

INTRODUCTION

Nature uses iron-sulfur clusters in various metalloproteins to accept, store, redistribute, and donate electrons.[1] In addition, iron-sulfur clusters are used for chemical transformations, such as proton reduction (hydrogenases), interconversion of carbon monoxide and carbon dioxide (CO dehydrogenases), the insertion of carbon monoxide (acetyl coenzyme A synthetase), and the conversion of N_2 to ammonia (nitrogenases). Most of these enzyme active sites feature metals in addition to iron (heterometals), and particular attention has been given to Mo and V in nitrogenases,[2–5] and to Ni in hydrogenases and in the C cluster of anaerobic carbon monoxide dehydrogenases (CODH).[6–11] Each enzyme uses a complex series of biosynthetic transformations to install a specific metal, which implies that the heterometal is advantageous though the specific advantage and its mechanism may be difficult to elucidate.[5,12] Potential reasons for the employment of heterometals include having specific interactions with the substrate, tuning the redox potential of the cluster, controlling the geometry, and/or forming bonds with other metals.

Determining the distribution of electrons in heterometallic clusters is a challenging but essential step in understanding their behavior. Chemists collect spectroscopic and crystallographic data and seek a self-consistent model for the electronic structure. Sometimes these data have led chemists to propose surprising metal oxidation states. For example, the C cluster of CODH undergoes a two-electron reduction from the C_{red1} state to the CO_2-binding C_{red2} state,[13,14] which is proposed to convert the Ni site from Ni^{2+} to "Ni^0" (Fig. 1, top).[15,16] This assignment is based on deconvolution of complex Mössbauer spectra of impure enzyme samples in the two states, which led to a model with no change in the iron oxidation states and therefore both electrons would go to nickel.[17,18] However, the presence of nickel(0) in a biological system is unprecedented, and in organometallic compounds generally requires the presence of neutral, π-acidic ligands like CO, PR_3, or *N*-heterocyclic carbenes (NHCs).[19] Further, having such a reduced center alongside Fe^{2+} and Fe^{3+} would typically redistribute electrons to avoid such a low oxidation state.[20] This idea is supported by synthetic analogues from Holm, in which addition of nickel(0) or nickel(I) species to a Fe_3 cluster leads to Fe_3Ni clusters in which two electrons are transferred to the iron sites to give tetrahedral or square planar nickel(II) site (Fig. 1, bottom).[21–24] In order to avoid proposing Ni^0 in C_{red2}, others have proposed that this site is Ni^{1+} or Ni^{2+}–H.[25–27] On the other hand, since low coordination numbers stabilise low oxidation states, the apparent three-coordinate environment of nickel in the crystallographic structure of C_{red2} might explain its anomalous ability to support a nickel(0) center.

Learning about the feasibility of unusual features of metalloenzymes can be addressed using synthetic reference compounds.[1] A specific challenge is the isolation of clusters that reproduce the three-coordinate nickel site that is seen in some crystallographic studies of reduced C cluster.[15] To our knowledge, these crystallographic studies of CODH are the only published examples of three-coordinate nickel in a cluster. Understanding such low-coordinate nickel sites could also have more general implications, because three-coordinate nickel has been proposed in intermediates of acetyl coenzyme A synthetase (ACS) as well (Fig. 1, top right).[11,28] This system has also been the source of controversy about the nickel oxidation state which is being addressed with artificial metalloproteins as models.[29,30] These examples demonstrate the need for reliable structural and spectroscopic characterization of biomimetic heterometallic clusters, which could provide principles that help to understand the influence of the heterometal.

In this work, we provide an isolable platform for understanding the electronic structure of low-coordinate, low-valent nickel sites that have geometric similarity to the C cluster of CODH. Specifically, we describe compounds with three-coordinate nickel in an iron-sulfur cluster for the first time. By using tungsten as a second heterometal, we stabilise WFe_2NiS_4 clusters at two oxidation levels, and elucidate their crystallographic and electronic structures. Interestingly, a simple one-electron change of the cluster results in a dramatic electronic structure reorganization from an $S = 7/2$ ground state in its reduced form to an $S = 0$ ground state in its oxidised form. X-ray absorption spectroscopy at the W, Fe, and Ni edges and spectroscopically calibrated DFT calculations show that the nickel valence in the clusters is better described as nickel(I) than as nickel(0). The cluster does not simply move the excess electron to other metal sites, but instead stores electrons in metal-metal bonds. The nature and extent of these M–M bonding electrons provide general lessons about the special abilities of heterometallic clusters, and establish principles that may guide the design of new clusters.

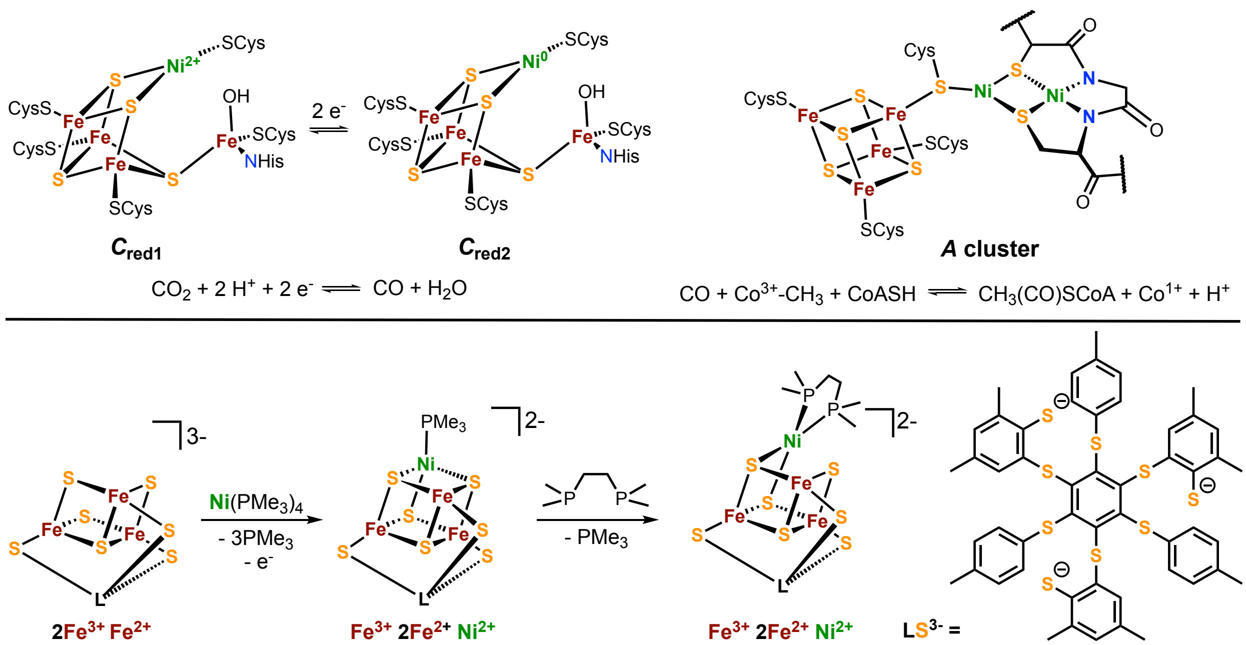

Figure 1. Top: Cofactors that feature nickel-iron-sulfur clusters. Left: C cluster intermediates of CO dehydrogenase that accumulate two electrons at the three-coordinate nickel site, as proposed by Jeoung and Dobbek.[15] Right: The *A* cluster of ACS featuring a proposed three-coordinate nickel site. Co^{3+}–CH_3 is a cobalt corrinoid enzyme. Bottom: Previously reported synthetic iron-sulfur clusters that feature Ni.

RESULTS

Synthesis and Structural Characterization of Clusters

The stepwise assembly of iron-sulfur clusters that incorporate heterometals is a longstanding challenge. One prominent approach has been to use ligands that pre-organise three iron sites into an incomplete cubane, and leave a fourth site available for the heterometal.[31–33] Using this strategy, Holm has synthesised the aforementioned Fe_3Ni clusters, which have Ni^{2+} in either tetrahedral or square planar geometries (Fig. 1, bottom).[21–23] These clusters exhibited complex EPR and Mössbauer spectra that were not interpreted in detail. We hypothesised that the studies on these clusters were limited by the inability to distinguish the three iron sites, which can have complex magnetic interactions. Therefore, we sought another scaffold that would give more easily isolable iron-sulfur clusters and a second heterometal that differentiates one of the cluster sites.

Guided by this strategy, we used the templating trisulfide anion $[Tp^*WS_3]^-$ (Tp* = tris(3,5-dimethyl-1-pyrazolyl)borate), which has been shown by Holm, Xu, and Agapie to give stepwise assembly of WFe, WFe_2, and WFe_3 clusters.[34–36] Additionally, to enforce the desired three-coordinate planar geometry at nickel, we required a cluster that creates a binding pocket for Ni but is resistant to formation of the complete cubane. To this end we prepared $[Et_4N][Tp^*WFe_2Cl_2S_3(\mu\text{-SMe})]$ (**WFe₂**, Fig. 2), which is closely related to ethylthiolate-bridged[35] and chloride-bridged[36] clusters in the literature. Complex **1** features a WFe_2S_3 core in which the two iron sites are bridged by a μ^2-thiolate group. In the crystallographic structure of **WFe₂**, the methyl group is disordered between *endo* and *exo* conformations (see Supplementary Material). The ^{1}H NMR spectrum has a 2:1 ratio of Tp* methyl integrations indicating C_s symmetry with the mirror plane containing W, Ni, and the SMe group.

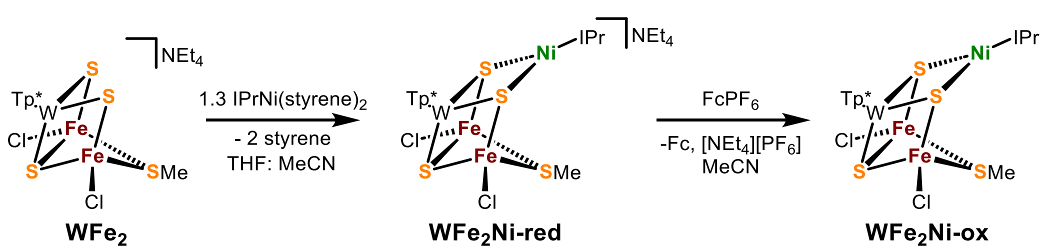

Figure 2. Synthetic route to complexes **WFe₂Ni-red** and **WFe₂Ni-ox**. IPr = 1,3-bis(2,6-diisopropyl)-1,3-dihydro-2*H*-imidazol-2-ylidene, Fc = ferrocene.

The addition of $IPrNi(styrene)_2$ (IPr = 1,3-bis(2,6-diisopropyl)-1,3-dihydro-2*H*-imidazol-2-ylidene) to **WFe₂** in a THF:MeCN mixture results in conversion to a new C_s species as indicated by a shift in the two diagnostic Tp* resonances in the ^{1}H NMR spectrum. X-ray crystallography shows that the product (**WFe₂Ni-red**) has a Ni site bound to two sulfides and the NHC, which is clearly three-coordinate as the Ni···SMe distance of 3.102(12) Å is too long to be a bond. This feature has some similarity to the structures of reduced forms of the NiFe CODH cofactor, which show Ni···μ^3-S distances around 3.53 Å.[15] Since **WFe_2Ni-red** provides the first example of a three-coordinate nickel site in a synthetic iron-sulfur cluster, it gives us an exciting opportunity to understand the properties of this kind of site.

There are several crystallographic structures of NiFe CODH, but each suffers from disorder near the nickel site and/or partial occupancy of metal sites.[37] Thus, **WFe_2Ni-red** offers the first high-precision look at a three-coordinate site in any iron-sulfur cluster. The nickel-sulfide distances are 2.1681(8) and 2.1775(8) Å, while the nickel-carbon distance is 1.951(3) Å. The nickel geometry is somewhat distorted from trigonal planar toward a T shape (sum of the angles is 359°), but the symmetry in the ^{1}H NMR spectrum and the DFT geometry optimization (described below) suggest that the movement of the NHC off the mirror plane is due to crystal packing. The Ni–Fe distances are 2.8814(6) and 2.7979(6) Å, which are longer than in Holm's Fe_3NiS_4 cubane clusters (Ni–$Fe_{average}$ = 2.689(5) Å).[21] Interestingly the W–Ni distance of 2.6216(5) Å could be classified as a single bond based on the formal shortness ratio[38] of 1.07, and the nature of the W-Ni interaction will be addressed in detail below.

The ability to compare **WFe_2** to **WFe_2Ni-red** also enables us to assess the influence of Ni on the rest of the cluster. Installation of Ni increases the average W–S distance from 2.312(1) Å to 2.364(1) Å, consistent with a lowering of W–S covalency upon coordination of the Ni (see below). Similarly, the average Fe–S distance increases slightly from 2.248(1) Å (**WFe_2**) to 2.294(1) Å (**WFe_2Ni-red**). The most dramatic change is in the Fe–Fe distance, which contracts from 2.6684(5) Å (**WFe_2**) to 2.5866(6) Å (**WFe_2Ni-red**).

Addition of the oxidant ferrocenium hexafluorophosphate to a MeCN solution of **WFe_2Ni-red** results in an immediate color change from dark red to dark yellow in the oxidised product (**WFe_2Ni-ox**). The ^{1}H NMR spectrum of **WFe_2Ni-ox** shows all resonances close to the diamagnetic region. X-ray crystal analysis (Fig. S16) shows that **WFe_2Ni-ox** retains the three-coordinate Ni site, but poor crystal quality and disorder prevent further discussion of bond metrics until the DFT calculations described below.

Spin States from Spectroscopy and Magnetometry

Mössbauer spectroscopy provides key information on iron oxidation states. The Mössbauer spectra of samples at 220 K are presented in Fig. 3 (spectra collected at 80 K are in the Supplementary Material). For **WFe_2**, the isomer shift of 0.51 mm s^{-1} is identical to the $Fe^{2.5+}$ sites in $[Fe_4S_4Cl_4]^{2-}$, indicating that **WFe_2** similarly has a delocalised mixed-valence pair of high-spin iron ions.[39,40] Installation of the nickel in **WFe_2Ni-red** results in a shift to $\delta = 0.58$ mm s^{-1}, which is much smaller than expected for a one-electron reduction of the [2Fe] fragment (predicted as +0.18 mm s^{-1} for 0.5 electrons per Fe).[24] Thus, the iron sites gain little electron density from nickel incorporation. Oxidation of **WFe_2Ni-red** to **WFe_2Ni-ox** results in a decrease of the isomer shift to 0.45 mm s^{-1}, and this larger change of –0.13 mm s^{-1} from **WFe_2Ni-red** to **WFe_2Ni-ox** is more consistent with a one-electron oxidation of the two-iron fragment to give a pair of high-spin Fe^{3+} sites.

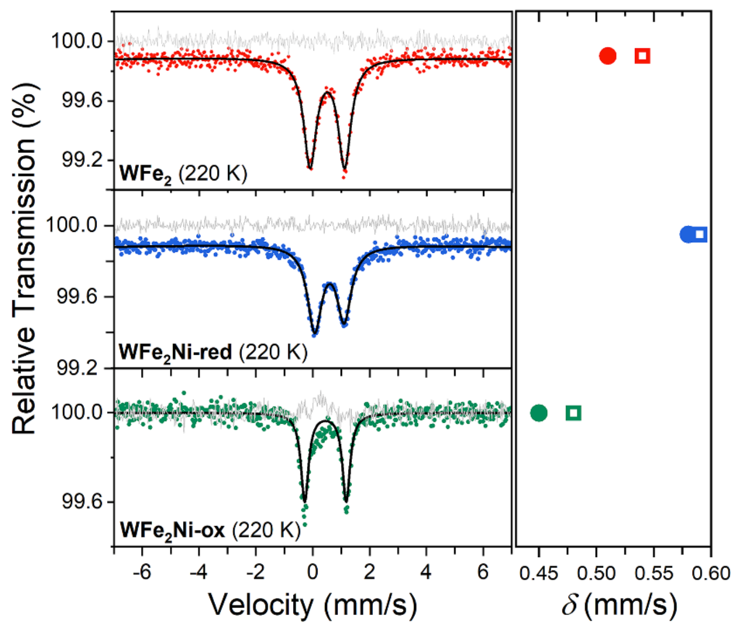

Figure 3. Overlay of the Mössbauer spectra of clusters at 220 K. Experimental δ values are plotted as filled circles and DFT computed δ values are plotted as open squares. **WFe_2**: δ = 0.51 mm s^{-1} (δ_{DFT} = 0.54 mm s^{-1}), $|\Delta E_Q|$ = 1.23 mm s^{-1}, Γ = 0.54 mm s^{-1}. **WFe_2Ni-red**: δ = 0.58 mm s^{-1} (δ_{DFT} = 0.59 mm s^{-1}), $|\Delta E_Q|$ = 1.03 mm s^{-1}, Γ = 0.51 mm s^{-1}. **WFe_2Ni-ox**: δ = 0.45 mm s^{-1} (δ_{DFT} = 0.48 mm s^{-1}), $|\Delta E_Q|$ = 1.45 mm s^{-1}, Γ = 0.32 mm s^{-1}.

The solid-state magnetic susceptibility of each compound was measured using variable-temperature SQUID magnetometry. For **WFe_2**, the $\chi_M T$ value of 7.14 cm^3K/mol at 300 K is consistent with an isolated S = 7/2 ground state, with g_{iso} = 1.90 and minimal zero-field splitting (Fig. 4a). The temperature dependence of $\chi_M T$ for **WFe_2Ni-red** is similar to that of **WFe_2**, and displays a $\chi_M T$ value of 6.84 cm^3K/mol at 300 K, again consistent with an S = 7/2 ground state (g_{iso} = 1.86). The X-band EPR spectra of **WFe_2** and **WFe_2Ni-red** are also similar (Fig. 4b). Using the S = 7/2 ground state determined from SQUID magnetometry, we simulated the spectra using the spin Hamiltonian $\hat{H} = D\hat{S}_z^2 + E(\hat{S}_x^2 - \hat{S}_y^2) + (g_x+g_y+g_z)\mu_B \boldsymbol{SH}$, where D and E are the axial and transverse zero-field splitting parameters, S_i ($i = x,y,z$) are the spin operators, and $g_{x,y,z}$ are the principal g-values. Fig. 4a shows the best simulations, which yielded the following parameters for **WFe_2**: $g_{x,y,z}$ = 2.10, 2.01, 2.00, D = 0.75 cm^{-1} and E = 0.18 cm^{-1}. The best simulation of **WFe_2Ni-red** yielded similar parameters, with $g_{x,y,z}$ = 2.16, 2.01, 2.00, D = 0.90 cm^{-1}, E = 0.21

cm^{-1}. Consistent with its NMR spectrum, **WFe$_2$Ni-ox** has no detectable X-band EPR spectrum and SQUID magnetometry shows it to be diamagnetic, with a low $\chi_M T$ value of 0.6 cm^{3}K/mol between 2–100 K attributed to a small paramagnetic impurity (a gradual increase at higher temperature indicates some population of excited states).

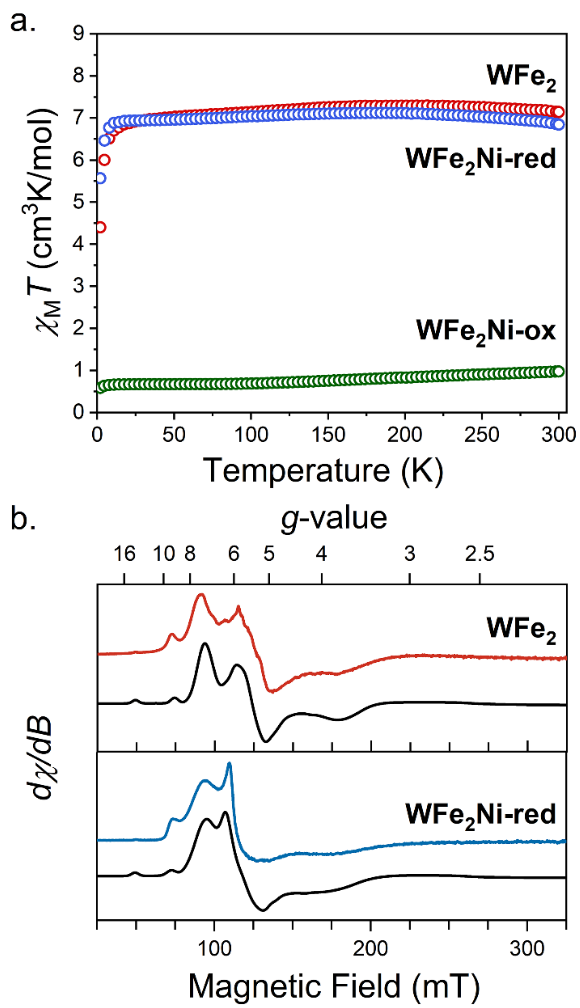

Figure 4. a. DC magnetic susceptibility data for **WFe$_2$**, **WFe$_2$Ni-red**, **and WFe$_2$Ni-ox** collected under an applied magnetic field of 0.1 T. b. EPR data for **WFe$_2$** and **WFe$_2$Ni-red** collected at 9.43 GHz and 5 K in an acetonitrile-toluene glass at 5 K.

The Mössbauer, SQUID, and EPR data enable the assignment of oxidation states and electron configurations in **WFe$_2$**. Double exchange within mixed-valent iron dimers is known to favor alignment of their unpaired spins (ferromagnetic coupling) to give S_{Fe2} = 9/2. Antiferromagnetic coupling between this spin subsystem and a high-spin W^{4+} ion (S_W = 1) yields the observed S = 7/2 ground state. This assignment can then be used as an anchor to explore spin-state assignments for the nickel-containing clusters. For

WFe_2Ni-red, maintaining the $Fe^{2.5+}{}_2$ mixed-valence pair leaves two possible assignments: $W^{4+}Fe^{2.5+}{}_2Ni^0$ or $W^{3+}Fe^{2.5+}{}_2Ni^{1+}$. Considering the short W–Ni distance as a bond, these models are distinguished by the nature of this bond: in the nickel(0) model this would be a dative bond (Ni→W) in which both electrons are formally assigned to the nickel, whereas in the nickel(I) model there is a covalent bond (Ni–W) where the electrons would be equally shared between metals. These are not distinguished by the techniques used above, and therefore we turned to X-ray absorption spectroscopy (XAS).

X-ray Absorption Spectroscopy

To refine the electronic structure descriptions of the three clusters, XAS was performed at the Fe and Ni K edges (1*s*→valence) and the W L_3 edge ($2p_{3/2}$→valence), and the spectra are presented in Fig. 5. The Fe K-pre-edge peaks at 7112 eV correspond to states with dominant local Fe 3*d* character, while to higher energy there is a dense continuum of states with metal-to-metal charge transfer (MMCT), Fe 4*p* and more delocalised character (Fig. 5, left). The Fe K-edge energies of 7117.4 eV (**WFe_2**), 7117.4 eV (**WFe_2Ni-red**) and 7118.2 eV (**WFe_2Ni-ox**) are consistent with the Fe oxidation state assignments from Mössbauer spectra described above. Additionally, the Fe pre-edge energy (Fig. S22) is only 0.09 eV different for **WFe_2** and **WFe_2Ni-red** which are assigned as $Fe^{2.5+}{}_2$, while it shifts +0.23 eV from **WFe_2Ni-red** to **WFe_2Ni-ox** indicating oxidation to $Fe^{3+}{}_2$.

Importantly, the Ni XAS of **WFe_2Ni-red** and **WFe_2Ni-ox** each show pre-edge features at 8330.8-8330.9 eV. The presence of low-energy pre-edge absorption *indicates that the Ni 3*d *manifold is partially unoccupied*, which is most consistent with a Ni^{1+} assignment. The presence of a pre-edge feature does not rule out a Ni^0 configuration, since previous studies have shown that pre-edge features can arise from strong π-backbonding, but those features generally fall at higher energy closer to the edge.[41,42] In the mid-edge region (8332–8342 eV), oxidation from **WFe_2Ni-red** to **WFe_2Ni-ox** results in a shift of 0.3–0.5 eV to higher energy without changing shape, suggesting a similar Ni coordination environment and electronic configuration but a somewhat lower electron density at the Ni nucleus. The W L_3 peaks fall within 0.3 eV, but due to a lack of reference data, analysis of the XAS data required DFT (density functional theory) computations, presented below.

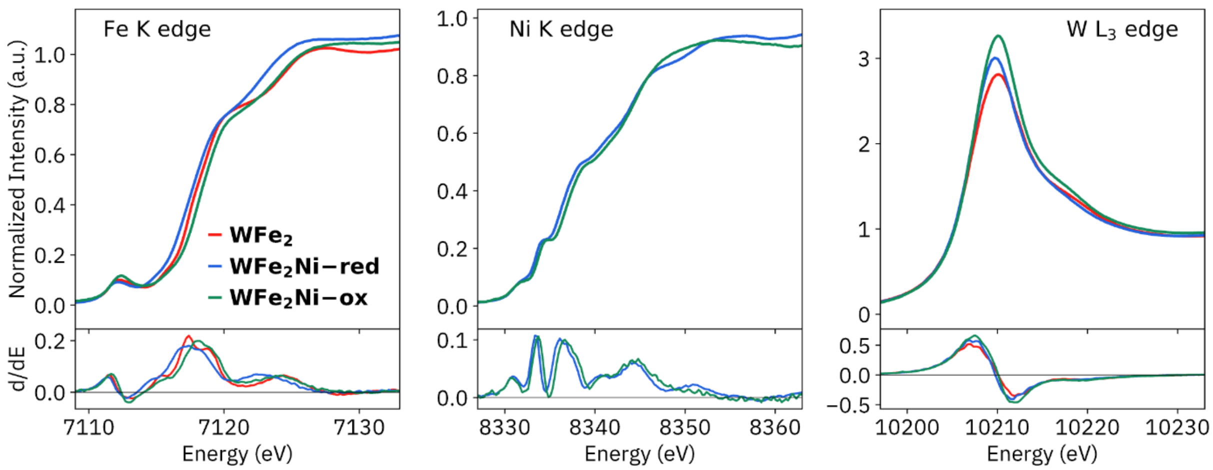

Figure 5. Normalised and flattened Fe K-edge (left) Ni K-edge (middle) and W L_3-edge (right) XAS spectra of **WFe$_2$**, **WFe$_2$Ni-red** and **WFe$_2$Ni-ox**, with derivative spectra below.

Computations

The clusters were investigated with broken-symmetry (BS) DFT calculations at the TPSSh/ZORA-def2-TZVP level, to explain the XAS spectra and to provide greater detail on the electronic structure (see the Supplementary Material for computational details). The optimised structures of are in good agreement with the available crystallographic data, with mean (absolute) errors in Fe–Fe, Fe–W and Ni–W distances of –0.046 (0.052) Å for **WFe$_2$** and **WFe$_2$Ni-red**, and only slight deviations from C_s symmetry as noted above. Qualitatively equivalent BS wavefunctions and properties were obtained using other functionals or H-optimised crystallographic coordinates. BS wavefunctions were analysed with Hirshfeld population analysis and Pipek-Mezey localization.[43–46] We first describe the distribution of *d* electrons in the clusters within this unrestricted single-determinant model before presenting the predicted Mössbauer isomer shifts and X-ray absorption spectra; the agreement of these predicted spectra with the experimental values provides evidence for the accuracy of the calculations. Most importantly, the calculations enable deeper analysis of the experimental spectra for resolving the electronic structure of the clusters.

Fig. 6 presents schematic representations of the *d*-electron distributions in the three clusters, both with artificial one-center localization (top) and with the inclusion of M–M bonding (bottom). In agreement with the interpretation of the experimental Mössbauer and X-ray spectroscopy, the DFT models of the clusters **WFe$_2$** and **WFe$_2$Ni-red** show a delocalised $Fe^{2.5+}_2$ subsystem with five occupied α *d*-orbitals at each Fe and one β Fe-Fe σ-bonding orbital, while **WFe$_2$Ni-ox** has an antiferromagnetically-coupled Fe^{3+}_2 subsystem.

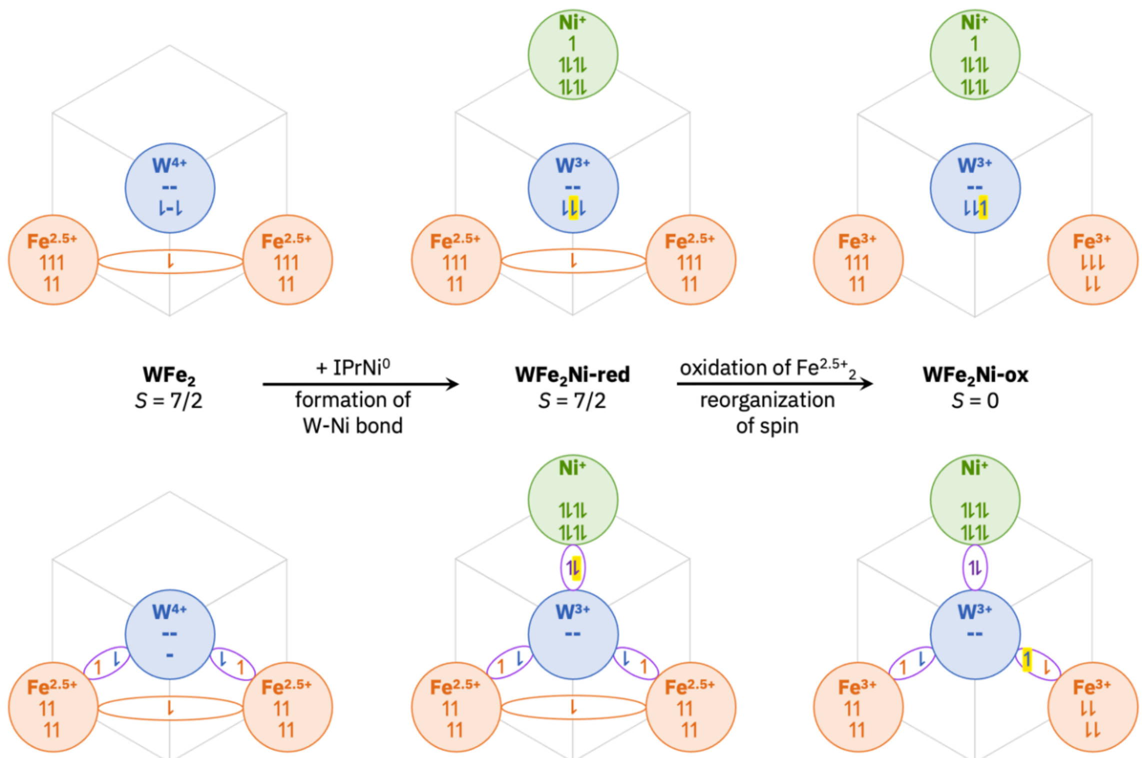

Figure 6. Schematic representations of the *d* electron assignments of the three clusters, in a forced local limit with M–M bonds treated as antiferromagnetic coupling (top) and as paired M–M bonding orbitals (bottom). The electrons in spin-polarised Fe–W bonds are colored to show their assignment in the local limit, while those in the Ni–W bond are not, to indicate the covalent, closed-shell character of the Ni–W bonds. For each reaction, the changing W electron is highlighted.

M–M bonds were identified and characterised by inspection of localised orbitals and the calculated α/β overlaps. Direct exchange between metal centers with opposing majority spins results in electronic structures that may be described within a continuum from weak antiferromagnetic coupling (characterised by local singly occupied orbitals with small α/β overlaps) to closed-shell covalent bonding (in which orbitals with α/β overlaps close to unity are delocalised across both metal centers). Intermediate overlaps may be described as spin-polarised covalent bonding or as strong antiferromagnetic coupling.

Importantly, the computations on **WFe$_2$Ni-red** and **WFe$_2$Ni-ox** show Ni–W σ interactions with α/β overlaps of 0.97–0.99, which indicate closed-shell bonds rather than separate centers with antiferromagnetic coupling. The M–M bonding orbitals of **WFe$_2$Ni-ox** are plotted in Fig. 7 and are representative of those of the other clusters as well. Because of the pairing of these α and β electrons, they do not contribute to the local spin at either metal. Thus, the nickel(I) character *does not* imply spin density at the nickel site: rather, the nickel(I) formation comes from equal sharing of the doubly occupied Ni–W bonding orbitals (in both

WFe_2Ni-red and **WFe_2Ni-ox**, the Ni–W bonds are only weakly polarised toward Ni, with roughly 62% Ni character). Stretching the Ni-W bond *in silico* results in heterolytic cleavage, yielding a reduced [**WFe_2**]$^-$ cluster and Ni^+NHC fragment (see Supplementary Material for details). This result supports the characterization of the Ni addition reaction as an electron transfer from Ni to W and the assignment of the Ni–W bond as covalent rather than dative. The other doubly occupied Ni *d* orbitals of **WFe_2Ni-red** and **WFe_2Ni-ox** lie almost completely on Ni, aside from weak spin polarization/σ interactions with the Fe centers (up to 8% Fe character for **WFe_2Ni-red**, 16% for **WFe_2Ni-ox**). Further, in each of the three clusters, the computations also show two spin-polarised Fe–W σ bonds with α/β overlaps of 0.80–0.88, which are formed from tungsten d_{xz} and d_{yz} orbitals (Fig. 7a-7d). In **WFe_2Ni-ox**, these bonds and the antiferromagnetic coupling between the Fe^{3+} centers result in a non-Hund configuration and zero local spin population at the formally d^3 W^{3+} center.[47] (Here, *non-Hund* indicates that there are orbitals on one atom that are singly occupied by electrons with opposite spin. Though Hund's first rule is strictly a rule about atomic multiplets, our use of *non-Hund* is meant as a qualitative description of the leading W^{3+} configuration within the BS wavefunction.)

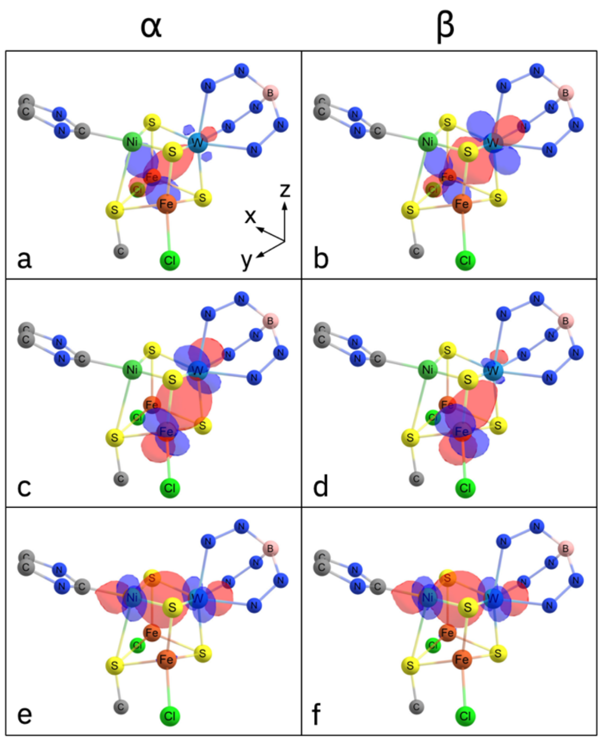

Figure 7. Fe–W (a–d) and Ni–W (e and f) bonding orbitals of **WFe_2Ni-ox**; aside from their spins, the M–M bonding orbitals of **WFe_2** and **WFe_2Ni-red** are very similar. Orbitals b and c, from which the non-Hund character at W is assigned, have a small overlap of 0.31 and their planes are oriented at approximately 90º. The Fe–W and Ni–W orbitals have α/β overlaps of 0.88 and 0.99, respectively. All H and most C atoms are omitted for clarity.

The strength of spin coupling and M–M bonding in **WFe_2Ni-ox** were also evaluated by calculating excited states that were targeted to eliminate specific M–M interactions (see Supplementary Material for details). The non-Hund character of **WFe_2Ni-ox** is found to be the net result of strong Fe–W (~26000 cm^{-1} or 74 kcal mol^{-1}) and Fe–Fe (2800–3900 cm^{-1} or 8–11 kcal mol^{-1}) interactions, which outcompete the weak exchange between the Fe-W bonding electrons (<1100 cm^{-1} or <3 kcal mol^{-1}). That is, the exchange energy lost due to local non-Hund character at tungsten is outweighed by the M–M bonds.

In summary, we assign formal oxidation states in the three clusters as $Fe^{2.5+}{}_2W^{4+}$ (**WFe_2**), $Fe^{2.5+}{}_2W^{3+}Ni^{1+}$ (**WFe_2Ni-red**), and $Fe^{3+}{}_2W^{3+}Ni^{1+}$ (**WFe_2Ni-ox**). Thus, the addition of $IPrNi^0$ to **WFe_2** to form **WFe_2Ni-red** involves an electron transfer from Ni^0 to W^{4+} with concomitant formation of a Ni–W covalent bond. The oxidation of **WFe_2Ni-red** to form **WFe_2Ni-ox** removes a delocalised β electron of the Fe_2 system, eliminating the double-exchange mechanism and changing the Fe–Fe coupling from ferromagnetic to antiferromagnetic. All three complexes have Fe–W bonds, and the bond in **WFe_2Ni-ox** synergises with the $Fe^{3+}{}_2$ antiferromagnetic coupling to give non-Hund character at W.

Computations on X-ray Absorption Spectra

Determining the electronic structure of iron-sulfur clusters is a challenging area with great importance for understanding these ubiquitous cofactors.[48] The DFT analysis in the prior section is validated by the accurate calculation of spectral properties from the DFT wavefunctions, in particular the observable spectral changes for the two reactions **WFe_2→WFe_2Ni-red** and **WFe_2Ni-red→WFe_2Ni-ox**. Calculated Mössbauer isomer shifts are in excellent agreement with experiment and correlate well with Fe Hirshfeld charges (Fig. 3, right panel; see Supplementary Material for details). TDDFT-calculated XAS transitions at all three edges are also highly accurate and offer further insight into the electronic structural features probed in the experiments (see Supplementary Material for further XAS analysis). Fe and Ni pre-edges are presented in Fig. 8 together with calculated spectra. The Fe pre-edges result from states with both local 3*d* and MMCT character, demonstrating the facile mixing of the metal 3*d* orbitals in the clusters. The Fe pre-edge peak energy shifts reflect the same changes in electron density at Fe that are observed in the Mössbauer spectra. The presence of Ni 3*d* character in the pre-edge states for both elements, including 21-27% Ni localization in the first Ni transitions, supports the description of Ni as having a significantly unoccupied 3*d* manifold (see Fig. 8 inset) and being best described as nickel(I).

The W L_3 peak energy shifts of –0.3 (**WFe_2→WFe_2Ni-red**) and +0.3 eV (**WFe_2Ni-red→WFe_2Ni-ox**) are well-reproduced by TDDFT at –0.3 and +0.2 eV, respectively (see Supplementary Material). Calculations on hypothetical complexes $[TpW^{3-5+}S_n(SH)_{3-n}]^{0/-}$ (n = 0, 1) indicate that the magnitudes of these energy shifts are reasonable for reactions with or without formal oxidation state change at W (see

Supplementary Materials for details). The accuracy of the calculated W L-edge shifts strongly supports the DFT models of the electronic structures, and underscores the importance of calculations in the interpretation of XAS in such covalent, polynuclear systems.

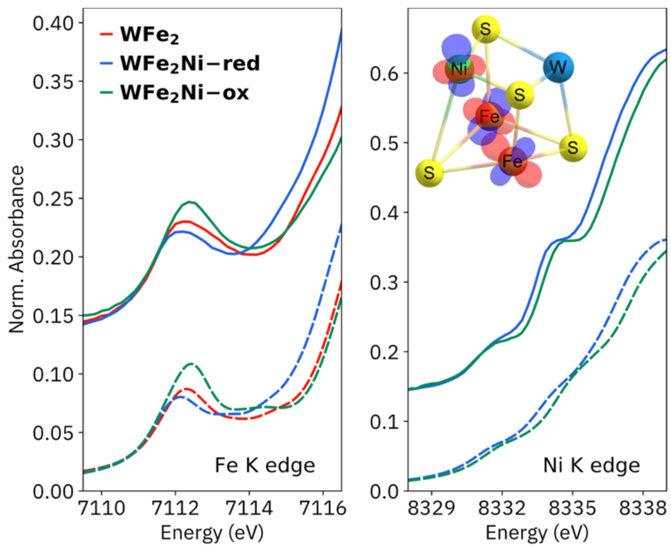

Figure 8. Experimental (solid lines) and calculated (dashed lines) Fe and Ni pre-edges of the three clusters, with the experimental spectra offset by 0.13 for clarity. The experimental (calculated) Fe pre-edge maxima are found at 7112.27 (7112.30) eV for **WFe_2**, 7112.18 (7112.14) eV for **WFe_2Ni-red** and 7112.40 (7112.43) eV for **WFe_2Ni-ox**. The natural transition orbital for the first Ni K-edge excited state, which accounts for most of the intensity of the first absorption feature, is localised 27% to Ni and 49% to the two Fe combined. It is plotted inset with an isovalue of 0.1 and all elements except metals and sulfur are omitted for clarity.

DISCUSSION

Three-coordinate nickel in an iron-sulfur cluster

One of the many intriguing aspects of the C cluster of carbon monoxide dehydrogenase (CODH) enzymes is the three-coordinate nickel site that has been proposed in both C_{red1} and C_{red2}, and which is proposed to be nickel(0) in C_{red2}.[15] Three-coordinate nickel is rare in natural systems, as nickel generally adopts four-, five-, or six-coordinate geometries in the presence of biological Lewis bases.[49] This abnormality has even led one group to reinterpret the crystallographic data for C_{red2} in terms of a model with a crystallographically invisible nickel-hydride that would give four-coordinate nickel(II).[25] To our knowledge, no spectroscopic evidence corroborates the three-coordinate nickel site in the C cluster, leaving a need for further verification of the capability of an iron-sulfur cluster to support three-coordinate nickel. Further, synthetic complexes with similar geometries enable comparison of nickel(I) and nickel(0) formulations.

Here we use synthetic complexes, which lack many of the difficulties of the CODH metalloproteins (potential heterogeneity, additional clusters, and lower-resolution crystallography), to gain more definitive insight into the geometric and electronic structure. Importantly, the "open cubane" shape of **WFe$_2$Ni-red** and **WFe$_2$Ni-ox** is closely analogous to the cage in the C cluster. The synthetic compounds are not perfect structural analogues, because they lack the dangling iron site, have tungsten substituted for one of the iron atoms, and have an NHC on the nickel in place of the natural cysteine. Despite these limitations, they do enable us to query the feasibility and properties of low-coordinate, low-valent nickel in a biomimetic environment. We know of no previous iron-sulfur clusters having a three-coordinate nickel site. Holm and coworkers have reported several iron-sulfur clusters with a nickel in one corner, but the nickel sites in these clusters were four-coordinate.[21–23] Here, we leverage the $[TpWS_3]^-$ scaffold to sequentially insert Fe and Ni sites into a sulfide cluster, and the steric shielding of an *N*-heterocyclic carbene (NHC) ligand stabilises a three-coordinate nickel site. This shows that three-coordinate nickel is feasible within an iron-sulfide cluster.

Electronic structure: tests of the nickel(0) hypothesis and metal-metal bonding

The spin-coupling pathways are complex in Fe_3S_4 clusters.[50–52] Here, we take advantage of tungsten substitution for one iron site to simplify the analysis and to enable us to query different nuclei using X-ray absorption spectroscopy. We started by thoroughly characterizing the oxidation states and electronic structure of the nickel-free precursor **WFe$_2$**, which has a mixed-valence $Fe^{2.5+}{}_2$ pair (S_{Fe2} = 9/2) antiferromagnetically coupled to high-spin W^{4+} (S_W = 1) to give an S_{total} = 7/2 ground state. Using this as a launching point, we added a nickel(0) source which gave another S_{total} = 7/2 species. The addition of nickel(0) gives a species with the same spin states and spin coupling, which might have been interpreted as the addition of a spin-inactive, d^{10} nickel(0) species. However, we observe pre-edge features that are characteristic of 1*s*→3*d* transitions, which requires significant depopulation of the 3*d* manifold. Formally d^{10} systems may exhibit sufficient transfer of 3*d* electrons to ligands via covalency or π-backbonding for the observation of pre-edge features with significant metal 3*d* character.[41,42,53] Thus, Ni XAS indicates significant charge-transfer from Ni into the **WFe$_2$** cluster which, given the available moieties as well as the Fe and W XAS, most likely proceeds as Ni–W bonding. At this point, two electronic structural descriptions may be considered: a Ni→W dative bond or a Ni–W covalent bond, the latter of which implies electron transfer to give formal oxidation states of nickel(I) and tungsten(III). We assign the Ni sites in **WFe$_2$Ni-red** and **WFe$_2$Ni-ox** as nickel(I) based on computational results: a Ni–W σ-bonding localised orbital is shared approximately equally between Ni and W and cleavage of the Ni–W bond *in silico* proceeds heterolytically to form a nickel(I) fragment. Even though the Ni^{1+} formulation is favored, it is important to note that the distinction between Ni^0 and Ni^{1+} is not exact or binary because either is compatible with the spectroscopy and assigned spin coupling of the clusters.

The oxidation of **WFe_2Ni-red** to **WFe_2Ni-ox** is Fe-centered, which is indicated by a similarity in Ni K-edges, a positive shift of the Fe K-edge and substantial increases in Fe pre-edge energy and intensity.[54] We tested this interpretation using broken-symmetry DFT studies, which reproduce all salient features of the various spectroscopic measurements and are thus "spectroscopically validated" in a way that lends credibility to the details of electronic structure that emerge from the calculations. Thus, the most appropriate oxidation state assignments are Ni^{1+} alongside $2Fe^{2.5+}$ and W^{3+} in **WFe_2Ni-red** or $2Fe^{3+}$ and W^{3+} in **WFe_2Ni-ox**. Interestingly, addition of Ni^0 to **WFe_2** results in the formal reduction of W and oxidation of Ni, and only a small increase in electron density at Fe (the isomer shift changes by only 0.07 mm s^{-1}). Thus, the W^{4+} site is the best electron acceptor for the electron from nickel(0), particularly because this enables the formation of a Ni–W bond.

Our DFT calculations show the presence of a two-electron Ni–W bond, which is equally shared between the metals. Lindahl has previously proposed a dative bond from nickel to the dangling iron, as a mechanism to stabilise a formal nickel(0) in the C_{red2} state of the C cluster.[55] In the clusters studied here, we indeed find metal-metal bonding, but it is better described as covalent interactions between the metals within the cube, and the formulation as a dative bond from d^{10} nickel(0) is disfavored by the computational results.

The tungsten ion also forms bonding interactions with the iron atoms, though these interactions are weaker. The Fe–W interactions in our precursor **WFe_2** may be compared to Holm's "cuboidal" $[LFe_3S_4]^{3-}$ cluster (Fig. 1, bottom left), which has been described as a valence delocalised $Fe^{2.5+}{}_2$ system antiferromagnetically coupled to an Fe^{3+} site; thus it is like **WFe_2** but with Fe^{3+} in place of W^{4+}. However, there is much less bonding character between $Fe^{2.5+}$ and Fe^{3+}, with α/β overlaps of ~0.3 as compared to ~0.8 for the Fe–W bonding orbitals of **WFe_2**. Overall, the tungsten site plays a dominant role in the metal-metal bonding within the new clusters due to the more extended orbitals of the 5*d* metal, and the greater orbital overlap can be visualised in the orbitals in our DFT computations.

Non-Hund configuration at W and generality to other clusters

The strong M–M bonding observed in the present clusters and the non-Hund character of **WFe_2Ni-ox** are closely connected. The combination of Fe–W bonding and antiferromagnetic interactions within the $Fe^{3+}{}_2$ unit overcome the exchange energy lost due to antiparallel spin alignment at W to produce a non-Hund electron configuration.[47] Both the strength of M–W bonding and lowering of the W *d* exchange energy are enabled by the more diffuse *d* orbitals of the 5*d* transition metal.[56] Similar M–M bonding and magnetic exchange interactions have been studied in 3*d*/4*d* substituted systems. This is related to a recently published system in which short Ni–Mo and Ni–W bonds were assigned as Ni^{1+}–M^{5+} (M = Mo, W) and the odd electrons pair up into a metal-metal bond like the ones described here.[57,58] Additionally, a computational study compared the exchange interactions in linear Ni_3, Ni_2Pd and Pd_3 complexes, demonstrating that the more diffuse *d* orbitals of Pd compared to Ni resulted in stronger antiferromagnetic coupling. As in the system here, the coupling was mediated by increased M–M σ-bonding interactions as well as lowered intra-site exchange that stabilised local non-Hund configurations.[59,60] Increased M–M covalency was also found in a study of the FeMo versus FeV cofactors of nitrogenase, as well as $MoFe_3$ versus VFe_3 model clusters.[61] Both the molybdenum cofactor and complex possess non-Hund character at Mo, while the vanadium analogues do not.[61,62] Unlike **WFe₂Ni-ox**, in which the non-Hund W results from only two Fe–W bonds while the Ni–W bond contributes no spin, the Mo clusters express a non-Hund configuration arising from Mo bonding to all three Fe sites: two in a delocalised $Fe^{2.5+}{}_2$ system and one antiferromagnetically-coupled Fe^{3+}.

Since M–M bonding is maximised with heavier metals, are such bonds likely to be relevant in the natural C cluster of CODH that is composed of iron and nickel? Bonding interactions similar to those in **WFe_2Ni-red** and **WFe_2Ni-ox** have been reported between 3*d* metals in the dimeric d^9-d^9 complex $[IPrNiCl]_2$, indicating that heavier *d*-block metals are not required for such interactions.[63,64] Further, a bimetallic complex featuring low-spin Ni^0 in proximity to a high-spin Fe^{3+} was found to have a bond order of 0.48 with a small amount of covalency in the interaction.[65] Future work will test for closed shell M–M bonding interactions in clusters having *only* 3*d* metals with biologically relevant coordination environments.

Finally, we mention several other implications for the broader set of heterometallic clusters. Both **WFe_2Ni-red** and **WFe_2Ni-ox** demonstrate the ability of clusters to leverage M–M interactions to stabilise low metal oxidation states (Ni^{1+}) in proximity to higher ones (Fe^{3+}). In this sense, the M–M bond stores electrons, and this might explain why metalloenzymes so often use clusters with short M–M distances for challenging reductions of molecules like N_2 and CO_2. The crystallographic model of the C cluster of CODH at -600 mV (proposed to be the C_{red2} state) features two short Ni···Fe distances: one that is close to the Fe atom with which it forms a rhomb in the Fe_3S_4 subcluster (Ni···Fe distance of 2.62 Å) and another with the dangling Fe atom (Ni···Fe_u distance of 2.87 Å). Additionally, there are unusually short (~2.6 Å) Fe···Fe distances in the FeMoco and FeVco, which could possibly engender M–M bonds in reduced states of the cofactor.[66] Some of us have proposed that Mo forms stronger metal-metal bonds than V in the nitrogenase active-site cluster.[61,67] Though this is not the only impact of heterometals on the different isoforms of nitrogenase,[5,68,69] it demonstrates the influence the heterometal can have on the electronic structures of active-site clusters.

Spin-state changes and electron storage in biological clusters

The spin state is a key determinant of reactivity in the active sites of metalloenzymes. In particular, Shaik has popularised the concept of exchange-enhanced reactivity, in which certain spin states have lower barriers that lead to faster reactions.[70] Such dramatic changes in spin states upon one electron redox changes in iron-sulfur clusters have also been proposed to gate electron transfer events.[71] In this context, the oxidation of **WFe_2Ni-red** to form **WFe_2Ni-ox** is notable because this one-electron change gives a massive rearrangement of the spin coupling scheme, resulting in change of the total spin from $S = 7/2$ to $S = 0$. The dominant factor in this spin-state change is the diiron unit within the cluster. When this unit is at the $Fe^{2.5+}{}_2$ level, the sharing of one β electron between the two sites leads to complete delocalization and a subset spin of $S_{Fe2} = 9/2$. One-electron oxidation to $Fe^{3+}{}_2$ leads to $S_{Fe2} = 0$ within this unit. To our knowledge, the closest analogue is the $S = 9/2 \leftrightarrow S = 0$ transition observed in the Fe_2S_2 cluster of serine-substituted ferredoxin.[72] Clusters **WFe_2Ni-red** and **WFe_2Ni-ox** provide the first experimental Fe XAS comparison of delocalised ($S = 9/2$) $Fe^{2.5+}{}_2$ to $Fe^{3+}{}_2$ without the complication of additional Fe sites.

The $S_{Fe2} = 9/2$ subsystem in **WFe_2** and **WFe_2Ni-red** is the net result of many spin coupling mechanisms. First, considering only the two Fe sites, double exchange (ferromagnetic coupling) competes with superexchange through diamagnetic sulfides (antiferromagnetic coupling) and vibronic coupling (favoring spin localization). In all reported synthetic Fe_2S_2 clusters, superexchange and vibronic coupling dominate, resulting in local Fe^{3+} and Fe^{2+} sites and $S = 1/2$ ground states (although substitution with heavier chalcogenides has been shown to stabilise higher spin ground states).[73] In **WFe_2** and **WFe_2Ni-red**, the combination of Fe-W covalent bonding (i.e., strong antiferromagnetic coupling between Fe and W *d* electrons) and exchange between the W 5*d* electrons instead aligns the spins on the two iron sites. It is this additional W-mediated pathway that is likely responsible for the dominance of ferromagnetic coupling of the iron ions, giving the $S_{Fe2} = 9/2$ subsystem. The energetic contribution of this pathway is limited to that of the weaker of its component interactions, namely the exchange between the W 5*d* electrons. From our analysis of the Hund ↔ non-Hund transition at W^{3+} in **WFe_2Ni-red** and **WFe_2Ni-ox**, we estimate the W-mediated coupling mechanism contributes <1100 cm^{-1} to the formation of the high-spin ground states. In this context, it is of interest to note that previous calculations on a Ga-substituted model of the FeMoco cluster of nitrogenase have estimated that the non-Hund configuration at Mo provides ~2100 cm^{-1} of stabilization energy.[62] In the oxidation from **WFe_2Ni-red** to **WFe_2Ni-ox**, the Fe-Fe double exchange mechanism is lost and Fe-Fe antiferromagnetic coupling outcompetes the W 5*d* exchange, resulting in a $S_{Fe2} = 0$ subsystem. These observations emphasise the delicate balance between competing spin coupling pathways in Fe-S systems.

Finally, we return to the C cluster of CODH. A conundrum in the Ni-CODH literature is that both C_{red1} and C_{red2} possess $S = 1/2$ ground states which implies that both states have similar electronic configurations and spin-coupling schemes.[13,14] Although C_{red2} is two electrons more reduced than C_{red1}, it remains unclear where these electrons localise to give an S = 1/2 ground state. Interpretation of the Mössbauer spectra is made challenging by the presence of additional iron-sulfur clusters in the enzymes, as well as sample heterogeneity.[17,18] In order to explain the same spin state with two-electron reduction, practitioners have proposed that the nickel site is diamagnetic, either as a nickel(II)-hydride, a nickel(0) center, or a Ni–Fe bonding interaction that would not significantly perturb the spin coupling scheme.[14,22,38] Here, a topologically related system indicates that closed shell bonding interactions between nickel and a nearby metal can maintain the spin coupling. Thus, it is possible that analogous interactions between the nickel and a cluster iron may house the additional electrons. However, metal-metal interactions in the C cluster are likely to be weaker than those observed in **WFe_2Ni-red** and **WFe_2Ni-ox**, because they use a 3*d* rather than a 5*d* metal.

Conclusions

We describe the first iron-sulfur clusters containing nickel with only three ligand donor atoms, which is a coordination environment similar to that proposed for Ni in intermediates of carbon monoxide dehydrogenase but not previously demonstrated in a well-characterised synthetic compound. In two different oxidation levels of the cluster, the nickel has little spin density but this does not necessarily imply nickel(0); rather it can result from a nickel(I) center that has a covalent bond to a nearby tungsten. These results provide experimental verification that heterometallic clusters can store electrons in metal–metal bonds to avoid low oxidation states (in this case Ni^0) that are generally difficult to stabilise with biologically available ligands. Further, in the case of the oxidised cluster, a non-Hund configuration of tungsten is observed in which orbitals are singly occupied by electrons with opposite spin. This unusual electron configuration is energetically compensated by forming strong metal–metal bonds. Finally, we demonstrate that removal of a single electron from the cluster results in a dramatic $S = 7/2$ to $S = 0$ spin-state change.

Acknowledgments

We acknowledge the Max Planck Society, the National Institutes of Health (GM-065313 to P.L.H.; F32-GM136179 to M.S.F), and the Deutsche Forschungsgemeinschaft (DE 1877/1-2 to S.D.) for funding. Use of the Stanford Synchrotron Radiation Lightsource (SSRL) at SLAC National Accelerator Laboratory is supported by the U.S. Department of Energy, Office of Science, Office of Basic Energy Sciences, under contract no. DE-AC02-76SF00515. We thank SSRL, the Deutsches Elektronen-Synchrotron, Christian Feike and beamline scientists for assistance with XAS. We thank Theodor Agapie, who developed similar clusters in independent research, for willingness to discuss pre-publication data. We thank Frank Neese for helpful discussion regarding the computations, Ragnar Bjornsson for discussions and for recalibration of the Mössbauer isomer shift for ORCA 5, Nicolas Dwarica for assistance with nickel precursor synthesis, and Nicholas Bingham and Peter Schiffer for assistance and equipment for magnetometry measurements.

Author Contributions

D.W.N.W. and M.S.F. conceived the research concept. D.W.N.W. performed the synthetic work. M.S.F. did the magnetic susceptibility and EPR studies. Z.M. did the X-ray absorption spectroscopy and computational work. B.Q.M. performed crystallographic studies. S.D. and P.L.H. directed the research. All authors wrote and edited the manuscript.

Data Availability Statement

Crystallographic data have been deposited at the Cambridge Crystallographic Data Centre, with deposition numbers 2267936 (**WFe_2**), 2267937 (**WFe_2Ni-red**) and 2267938 (**WFe_2Ni-ox**). All other relevant data generated and analysed during this study, which include experimental, spectroscopic and computational data, are included in this article and its Supplementary Information files.

REFERENCES

1. Beinert, H., Holm, R. H. & Münck, E. Iron-Sulfur Clusters: Nature's Modular, Multipurpose Structures. *Science* **277**, 653–659 (1997).
2. Einsle, O. & Rees, D. C. Structural Enzymology of Nitrogenase Enzymes. *Chem. Rev.* **120**, 4969–5004 (2020).
3. Van Stappen, C. *et al.* The Spectroscopy of Nitrogenases. *Chem. Rev.* **120**, 5005–5081 (2020).
4. Seefeldt, L. C. *et al.* Reduction of Substrates by Nitrogenases. *Chem. Rev.* **120**, 5082–5106 (2020).
5. Jasniewski, A. J., Lee, C. C., Ribbe, M. W. & Hu, Y. Reactivity, Mechanism, and Assembly of the Alternative Nitrogenases. *Chem. Rev.* **120**, 5107–5157 (2020).
6. Drennan, C. L., Doukov, T. I. & Ragsdale, S. W. The metalloclusters of carbon monoxide dehydrogenase/acetyl-CoA synthase: a story in pictures. *J. Biol. Inorg. Chem.* **9**, 511–515 (2004).
7. Ribbe, M. W. Insights into the Mechanism of Carbon Monoxide Dehydrogenase at Atomic Resolution. *Angew. Chem. Int. Ed.* **54**, 8337–8339 (2015).
8. Hegg, E. L. Unraveling the Structure and Mechanism of Acetyl-Coenzyme A Synthase. *Acc. Chem. Res.* **37**, 775–783 (2004).
9. Kampa, M., Pandelia, M.-E., Lubitz, W., van Gastel, M. & Neese, F. A Metal–Metal Bond in the Light-Induced State of [NiFe] Hydrogenases with Relevance to Hydrogen Evolution. *J. Am. Chem. Soc.* **135**,

3915–3925 (2013).

10. Ogata, H., Lubitz, W. & Higuchi, Y. Structure and function of [NiFe] hydrogenases. *J. Biochem.* **160**, 251–258 (2016).
11. Can, M., Armstrong, F. A. & Ragsdale, S. W. Structure, Function, and Mechanism of the Nickel Metalloenzymes, CO Dehydrogenase, and Acetyl-CoA Synthase. *Chem. Rev.* **114**, 4149–4174 (2014).
12. Britt, R. D., Rao, G. & Tao, L. Bioassembly of complex iron–sulfur enzymes: hydrogenases and nitrogenases. *Nature Rev. Chem.* **4**, 542–549 (2020).
13. Lindahl, P. A., Münck, E. & Ragsdale, S. W. CO dehydrogenase from Clostridium thermoaceticum. EPR and electrochemical studies in CO_2 and argon atmospheres. *J. Biol. Chem.* **265**, 3873–3879 (1990).
14. Spangler, N. J. *et al.* Substitution of Valine for Histidine-265 in Carbon Monoxide Dehydrogenase from *Rhodospirillum rubrum* Affects Activity and Spectroscopic States. *J. Biol. Chem.* **273**, 4059–4064 (1998).
15. Jeoung, J.-H. & Dobbek, H. Carbon Dioxide Activation at the Ni,Fe-Cluster of Anaerobic Carbon Monoxide Dehydrogenase. *Science* **318**, 1461–1464 (2007).
16. Lindahl, P. A. The Ni-Containing Carbon Monoxide Dehydrogenase Family: Light at the End of the Tunnel? *Biochemistry* **41**, 2097–2105 (2002).
17. Hu, Z. *et al.* Nature of the C-Cluster in Ni-Containing Carbon Monoxide Dehydrogenases. *J. Am. Chem. Soc.* **118**, 830–845 (1996).
18. Lindahl, P. A., Ragsdale, S. W. & Münck, E. Mössbauer study of CO dehydrogenase from Clostridium thermoaceticum. *J. Biol. Chem.* **265**, 3880–3888 (1990).
19. Hazari, N., Melvin, P. R. & Beromi, M. M. Well-defined nickel and palladium precatalysts for cross-coupling. *Nature Rev. Chem.* **1**, 0025 (2017).
20. Brown, A. C., Thompson, N. B. & Suess, D. L. M. Evidence for Low-Valent Electronic Configurations in Iron–Sulfur Clusters. *J. Am. Chem. Soc.* **144**, 9066–9073 (2022).
21. Ciurli, S., Ross, P. K., Scott, M. J., Yu, S. B. & Holm, R. H. Synthetic nickel-containing heterometal cubane-type clusters with $NiFe_3Q_4$ cores (Q = sulfur, selenium). *J. Am. Chem. Soc.* **114**, 5415–5423 (1992).
22. Zhou, J., Raebiger, J. W., Crawford, C. A. & Holm, R. H. Metal Ion Incorporation Reactions of the Cluster $[Fe_3S_4(LS_3)]^{3-}$, Containing the Cuboidal $[Fe_3S_4]^0$ Core. *J. Am. Chem. Soc.* **119**, 6242–6250 (1997).
23. Panda, R., Berlinguette, C. P., Zhang, Y. & Holm, R. H. Synthesis of MFe_3S_4 Clusters Containing a Planar M^{II} Site (M = Ni, Pd, Pt), a Structural Element in the C-Cluster of Carbon Monoxide Dehydrogenase. *J. Am. Chem. Soc.* **127**, 11092–11101 (2005).

24. Venkateswara Rao, P. & Holm, R. H. Synthetic Analogues of the Active Sites of Iron−Sulfur Proteins. *Chem. Rev.* **104**, 527–560 (2004).

25. Amara, P., Mouesca, J.-M., Volbeda, A. & Fontecilla-Camps, J. C. Carbon Monoxide Dehydrogenase Reaction Mechanism: A Likely Case of Abnormal CO_2 Insertion to a Ni−H Bond. *Inorg. Chem.* **50**, 1868–1878 (2011).

26. Breglia, R. *et al.* First-Principles Calculations on Ni,Fe-Containing Carbon Monoxide Dehydrogenases Reveal Key Stereoelectronic Features for Binding and Release of CO_2 to/from the C-Cluster. *Inorg. Chem.* **60**, 387–402 (2021).

27. Liao, R.-Z. & Siegbahn, P. E. M. Energetics for the Mechanism of Nickel-Containing Carbon Monoxide Dehydrogenase. *Inorg. Chem.* **58**, 7931–7938 (2019).

28. Can, M., Giles, L. J., Ragsdale, S. W. & Sarangi, R. X-ray Absorption Spectroscopy Reveals an Organometallic Ni–C Bond in the CO-Treated Form of Acetyl-CoA Synthase. *Biochemistry* **56**, 1248–1260 (2017).

29. Manesis, A. C., Yerbulekova, A., Shearer, J. & Shafaat, H. S. Thioester synthesis by a designed nickel enzyme models prebiotic energy conversion. *Proc. Natl. Acad. Sci. USA* **119**, e2123022119 (2022).

30. Kisgeropoulos, E. C., Manesis, A. C. & Shafaat, H. S. Ligand Field Inversion as a Mechanism to Gate Bioorganometallic Reactivity: Investigating a Biochemical Model of Acetyl CoA Synthase Using Spectroscopy and Computation. *J. Am. Chem. Soc.* **143**, 849–867 (2021).

31. Holm, R. H. & Lo, W. Structural Conversions of Synthetic and Protein-Bound Iron–Sulfur Clusters. *Chem. Rev.* **116**, 13685–13713 (2016).

32. Brown, A. C. & Suess, D. L. M. An Open-Cuboidal [Fe_3S_4] Cluster Characterized in Both Biologically Relevant Redox States. *J. Am. Chem. Soc.* **145**, 2075–2080 (2023).

33. McSkimming, A., Sridharan, A., Thompson, N. B., Müller, P. & Suess, D. L. M. An $[Fe_4S_4]^{3+}$–Alkyl Cluster Stabilized by an Expanded Scorpionate Ligand. *J. Am. Chem. Soc.* **142**, 14314–14323 (2020).

34. Scott, A. G. & Agapie, T. Synthesis of a Fe_3–Carbyne Motif by Oxidation of an Alkyl Ligated Iron–Sulfur (WFe_3S_3) Cluster. *J. Am. Chem. Soc.* **145**, 2–6 (2023).

35. Xu, G. *et al.* Ligand metathesis as rational strategy for the synthesis of cubane-type heteroleptic iron–sulfur clusters relevant to the FeMo cofactor. *Proc. Natl. Acad. Sci. USA* **115**, 5089–5092 (2018).

36. Zheng, B., Chen, X.-D., Zheng, S.-L. & Holm, R. H. Selenium as a Structural Surrogate of Sulfur: Template-Assisted Assembly of Five Types of Tungsten–Iron–Sulfur/Selenium Clusters and the Structural Fate of Chalcogenide Reactants. *J. Am. Chem. Soc.* **134**, 6479–6490 (2012).

37. Kung, Y. & Drennan, C. L. A role for nickel–iron cofactors in biological carbon monoxide and carbon dioxide utilization. *Curr. Opin. Chem. Biol.* **15**, 276–283 (2011).

38. Cotton, F. A. Chromium Compounds. In *Multiple Bonds Between Metal Atoms*, Eds. F. A. Cotton, C.

A. Murillo, R. A. Walton (Springer, 2005).

39. Silver, J. *et al.* Effects of Temperature and Pressure on the Mössbauer Spectra of Models for the [4Fe-4S]$^{2+}$ Clusters of Iron−Sulfur Proteins and the Structure of $[PPh_4]_2[Fe_4S_4(SCH_2CO_2C_2H_5)_4]$. *Inorg. Chem.* **38**, 4256–4261 (1999).
40. Scott, T. A., Berlinguette, C. P., Holm, R. H. & Zhou, H.-C. Initial synthesis and structure of an all-ferrous analogue of the fully reduced $[Fe_4S_4]^0$ cluster of the nitrogenase iron protein. *Proc. Natl. Acad. Sci. USA* **102**, 9741–9744 (2005).
41. Bein, Thomas. *et al.* Intrazeolite chemistry of nickel(0) complexes and Ni(0,II) clusters studied by EXAFS, solid-state NMR and FT-IR spectroscopy. *J. Am. Chem. Soc.* **110**, 1801–1810 (1988).
42. Desnoyer, A. N. *et al.* The Importance of Ligand-Induced Backdonation in the Stabilization of Square Planar d^{10} Nickel π-Complexes. *Chem. Eur. J.* **25**, 5259–5268 (2019).
43. Hirshfeld, F. L. Bonded-atom fragments for describing molecular charge densities. *Theoret. Chim. Acta* **44**, 129–138 (1977).
44. Lu, T. & Chen, F. Multiwfn: A multifunctional wavefunction analyzer. *Journal of Computational Chemistry* **33**, 580–592 (2012).
45. Pipek, J. & Mezey, P. G. A fast intrinsic localization procedure applicable for ab initio and semiempirical linear combination of atomic orbital wave functions. *J. Chem. Phys.* **90**, 4916–4926 (1989).
46. Liu, Z., Lu, T. & Chen, Q. An sp-hybridized all-carboatomic ring, cyclo[18]carbon: Electronic structure, electronic spectrum, and optical nonlinearity. *Carbon* **165**, 461–467 (2020).
47. Malrieu, J. P., Caballol, R., Calzado, C. J., de Graaf, C. & Guihéry, N. Magnetic Interactions in Molecules and Highly Correlated Materials: Physical Content, Analytical Derivation, and Rigorous Extraction of Magnetic Hamiltonians. *Chem. Rev.* **114**, 429–492 (2014).
48. Sharma, S., Sivalingam, K., Neese, F. & Chan, G. K.-L. Low-energy spectrum of iron–sulfur clusters directly from many-particle quantum mechanics. *Nature Chem* **6**, 927–933 (2014).
49. Halcrow, M. A. & Christou, G. Biomimetic Chemistry of Nickel. *Chem. Rev.* **94**, 2421–2481 (1994).
50. Sanakis, Y. *et al.* Evidence for Antisymmetric Exchange in Cuboidal [3Fe−4S]$^+$ Clusters. *J. Am. Chem. Soc.* **122**, 11855–11863 (2000).
51. Macedo, A. L., Moura, I., Moura, J. J. G., Le Gall, J., & Huynh Boi Hanh. Temperature-dependent proton NMR investigation of the electronic structure of the trinuclear iron cluster of the oxidized *Desulfovibrio gigas* ferredoxin II. *Inorg. Chem.* **32**, 1101–1105 (1993).
52. Mouesca, J.-M., Noodleman, L., Case, D. A. & Lamotte, B. Spin Densities and Spin Coupling in Iron-Sulfur Clusters: A New Analysis of Hyperfine Coupling Constants. *Inorg. Chem.* **34**, 4347–4359 (1995).

53. Tomson, N. C. *et al.* Re-evaluating the Cu K pre-edge XAS transition in complexes with covalent metal–ligand interactions. *Chem. Sci.* **6**, 2474–2487 (2015).
54. Kowalska, J. K. *et al.* X-ray Absorption and Emission Spectroscopic Studies of [$L_2Fe_2S_2$] Model Complexes: Implications for the Experimental Evaluation of Redox States in Iron-Sulfur Clusters. *Inorg. Chem.* **55**, 4485–4497 (2016).
55. Lindahl, P. A. Metal–metal bonds in biology. *J. Inorg. Biochem.* **106**, 172–178 (2012).
56. Kaupp, M. The role of radial nodes of atomic orbitals for chemical bonding and the periodic table. *J. Comput. Chem.* **28**, 320–325 (2007).
57. Rosenkoetter, K. E., Wojnar, M. K., Charette, B. J., Ziller, J. W. & Heyduk, A. F. Hydrogen-Atom Noninnocence of a Tridentate [SNS] Pincer Ligand. *Inorg. Chem.* **57**, 9728–9737 (2018).
58. Wojnar, M. K., Ziller, J. W. & Heyduk, A. F. Heterobimetallic and Heterotrimetallic Clusters Containing a Redox-Active Metalloligand. *Eur. J. Inorg. Chem.* **2017**, 5571–5575 (2017).
59. Tabookht, Z., López, X., Bénard, M. & Graaf, C. de. Isotropic Non-Heisenberg Behavior in $M_3(dpa)_4Cl_2$ Extended Metal Atom Chains. *J. Phys. Chem. A* **114**, 12291–12298 (2010).
60. Bastardis, R., Guihéry, N. & de Graaf, C. Isotropic non-Heisenberg terms in the magnetic coupling of transition metal complexes. *J. Chem. Phys.* **129**, 104102 (2008).
61. Rees, J. A. *et al.* Comparative electronic structures of nitrogenase FeMoco and FeVco. *Dalton Trans.* **46**, 2445–2455 (2017).
62. Bjornsson, R. *et al.* Identification of a spin-coupled Mo(III) in the nitrogenase iron-molybdenum cofactor. *Chem. Sci.* **5**, 3096–3103 (2014).
63. Dible, B. R., Sigman, M. S. & Arif, A. M. Oxygen-Induced Ligand Dehydrogenation of a Planar Bis-μ-Chloronickel(I) Dimer Featuring an NHC Ligand. *Inorg. Chem.* **44**, 3774–3776 (2005).
64. Lin, C.-Y. & Power, P. P. Complexes of Ni(I): a “rare” oxidation state of growing importance. *Chem. Soc. Rev.* **46**, 5347–5399 (2017).
65. Prat, J. R. *et al.* Bioinspired Nickel Complexes Supported by an Iron Metalloligand. *Inorg. Chem.* **59**, 14251–14262 (2020).
66. Spatzal, T. *et al.* Evidence for Interstitial Carbon in Nitrogenase FeMo Cofactor. *Science* **334**, 940–940 (2011).
67. Harris, D. F. *et al.* Mo-, V-, and Fe-Nitrogenases Use a Universal Eight-Electron Reductive-Elimination Mechanism To Achieve N2 Reduction. *Biochemistry* **58**, 3293–3301 (2019).
68. Moore, V. G., Tittsworth, R. C. & Hales, B. J. Construction and Characterization of Hybrid Component 1 from V-Nitrogenase Containing FeMo Cofactor. *J. Am. Chem. Soc.* **116**, 12101–12102 (1994).
69. Rebelein, J. G., Lee, C. C., Newcomb, M., Hu, Y. & Ribbe, M. W. Characterization of an M-Cluster-Substituted Nitrogenase VFe Protein. *mBio* **9**, e00310-18 (2018).

70. Shaik, S., Chen, H. & Janardanan, D. Exchange-enhanced reactivity in bond activation by metal–oxo enzymes and synthetic reagents. *Nature Chem.* **3**, 19–27 (2011).
71. Bominaar, E. L., Achim, C., Borshch, S. A., Girerd, J. J. & Munck, E. Analysis of Exchange Interaction and Electron Delocalization as Intramolecular Determinants of Intermolecular Electron-Transfer Kinetics. *Inorg Chem* **36**, 3689–3701 (1997).
72. Crouse, B. R., Meyer, J. & Johnson, M. K. Spectroscopic Evidence for a Reduced Fe_2S_2 Cluster with a S = 9/2 Ground State in Mutant Forms of *Clostridium pasteurianum* 2Fe Ferredoxin. *J. Am. Chem. Soc.* **117**, 9612–9613 (1995).
73. Henthorn, J. T., Cutsail, G. E., Weyhermüller, T. & DeBeer, S. Stabilization of intermediate spin states in mixed-valent diiron dichalcogenide complexes. *Nat. Chem.* **14**, 328–333 (2022).